



Electronic and Ionic Conductivity of $\text{La}_{0.95}\text{Sr}_{0.05}\text{Ga}_{0.95}\text{Mg}_{0.05}\text{O}_{3-\delta}$ (LSGM) Single Crystals

Ghislain M. Rupp,^{a,z} Michal Glowacki,^b and Jürgen Fleig^{a,*}

^aInstitute of Chemical Technologies and Analytics, Vienna University of Technology, Vienna AT-1060, Austria

^bInstitute of Physics, Polish Academy of Science, Warszawa PL-02668, Poland

The defect chemistry and charge transport properties of $\text{La}_{0.95}\text{Sr}_{0.05}\text{Ga}_{0.95}\text{Mg}_{0.05}\text{O}_{3-\delta}$ (LSGM) single crystals, grown by the Czochralski technique, were studied by impedance spectroscopy performed over a wide temperature range (180–800°C) and oxygen partial pressures from 0.21 to 1013 mbar. Owing to ion blocking Pt thin film electrodes impedance data showed a Warburg type 45° slope in the complex impedance plane. The spectra were analyzed by means of a generalized transmission line model which yielded the electronic and ionic conductivity, chemical and dielectric capacitance and the oxygen chemical diffusion coefficient. Activation energies for electronic (0.89 eV) and ionic charge transport (0.95 eV at low and 0.56 eV at high temperatures) were determined. Oxygen partial pressure dependent measurements revealed that the p-type conductivity is exactly proportional to $\text{pO}_2^{1/4}$ and that the ionic transference number approaches 1 for low oxygen partial pressures and low temperatures. Additional Hebb-Wagner type DC polarization experiments were carried out to determine the n- and p-type conductivities in a broad chemical potential range and to verify the results obtained by the AC impedance measurements.

© The Author(s) 2016. Published by ECS. This is an open access article distributed under the terms of the Creative Commons Attribution 4.0 License (CC BY, <http://creativecommons.org/licenses/by/4.0/>), which permits unrestricted reuse of the work in any medium, provided the original work is properly cited. [DOI: 10.1149/2.0591610jes] All rights reserved.

Manuscript submitted May 31, 2016; revised manuscript received August 5, 2016. Published August 18, 2016.

Strontium and magnesium doped lanthanum gallate (LSGM) has been widely investigated as potential electrolyte material in solid oxide fuel cells (SOFC) and thus as promising alternative to the fluorite type electrolytes yttria stabilized zirconia (YSZ) and gadolinium doped ceria (GDC). At lower temperatures (<700°C) the ionic conductivity of LSGM can exceed the conductivity of YSZ by more than a factor of 5^{1–3}. Although the ionic conductivity below ca. 600°C is smaller compared to GDC, LSGM has the advantage of a broad electrolytic domain with negligible electronic conductivity under typical reducing and oxidizing conditions of SOFCs.^{4,5} However, electrochemical properties of LSGM have been investigated almost exclusively on polycrystalline samples,^{1,6–11} in contrast to YSZ where many studies are also available on single crystals. This is largely because of the difficulty to synthesize larger single crystals of the preferred composition $\text{La}_{0.8}\text{Sr}_{0.2}\text{Ga}_{0.8}\text{Mg}_{0.2}\text{O}_{3-\delta}$ with sufficient quality. The very few existing studies on LSGM, mostly with lower dopant concentration, dealt with crystal structure, thermal conductivity and ionic conductivity.^{7,12} Detailed information on the electronic conductivity of LSGM single crystals is not available so far.

Measurements on polycrystalline materials often suffer from difficulties to discriminate between effects induced by grains and grain boundaries. In principle, impedance spectroscopy allows separation of resistive grain and grain boundary contributions and often a brick layer model is used for data analysis.^{13–15} However, this approach only works at lower temperatures (due to the limited frequency range of impedance spectroscopy) and for the total conductivity, which is largely ionic in LSGM. A separation of resistive bulk and grain boundary contributions of electrons in LSGM is highly non-trivial and electronic conductivities determined on polycrystals may not reflect true bulk properties. Also identification of fast conduction paths along grain boundaries fails in conventional impedance studies.¹⁶

Experiments on single crystals would reveal information on the bulk defect chemistry and the charge transport properties of the LSGM bulk, unaffected of any grain boundaries. Therefore, a $\text{La}_{0.95}\text{Sr}_{0.05}\text{Ga}_{0.95}\text{Mg}_{0.05}\text{O}_{3-\delta}$ single crystal grown by the Czochralski technique, was used in this study and investigated by impedance spectroscopy over a wide temperature (180–800°C) and oxygen partial pressure range (0.21–1013 mbar pO_2). Usage of ion blocking electrodes revealed information on bulk electronic and ionic conductivities of this LSGM composition. Data analysis is based on the general equivalent circuit model introduced in Ref. 17 by J. Jamnik and J. Maier for mixed ionic and electronic conductors (MIEC).

This very general model was successfully applied for the analysis of Pt|GDC|Pt¹⁸ and Ag|AgI|Ag₂S|AgI|Ag¹⁹ electrochemical cells and allows a detailed evaluation of the charge carrier properties and defect chemistry of MIECs. Complementary Hebb-Wagner type DC polarization experiments with one reversible $\text{La}_{0.6}\text{Sr}_{0.4}\text{CoO}_{3-\delta}$ electrode were carried out to determine both n- and p-type conductivities and to verify the results obtained by the AC impedance measurements.

Experimental

LSGM single crystal synthesis and substrate preparation.—The $\text{La}_{0.95}\text{Sr}_{0.05}\text{Ga}_{0.95}\text{Mg}_{0.05}\text{O}_{3-\delta}$ single crystal was grown by the Czochralski method using the following starting materials: La_2O_3 (4N purity), Ga_2O_3 (4N5 purity), SrCO_3 (4N5 purity) and MgO (4N purity). Reagents were dried for 6 hours—oxides at 1000°C and SrCO_3 at 300°C—before they were mixed in stoichiometric ratio and melted in an iridium crucible. A single crystal (20 mm ϕ , ~35 mm length) with convex crystal-melt interface was grown on (001) LaGaO_3 oriented seed with a pulling rate of 2.5 mm/h and a rotation speed of 20 rpm under ambient pressure in a nitrogen atmosphere. Then, the LSGM single crystal was cut into smaller specimen (5 × 5 × 0.5 mm³) by CrysTec GmbH (Germany) and the front and back side (001 oriented) of the single crystals were polished (epitaxy ready).

Sample preparation for AC impedance measurements.—A 400 nm Pt thin film was deposited on top of the as-prepared LSGM single crystals by a sputter coater (MED 020 Coating System, BAL-TEC, Germany) using a Pt (99.95% Pt, ÖGUSSA, Austria) target. Deposition was performed at room temperature in $2 \cdot 10^{-2}$ mbar Ar atmosphere and the film thickness was controlled during sputtering by a quartz micro-balance. After deposition the sample was turned and the sputter process was repeated to obtain a similar Pt thin film electrode on the back side. Finally, the side faces of the samples were grinded to remove any residual Pt. The microstructure of similarly prepared ~350 nm thin Pt films on top of yttria stabilized zirconia single crystals before and after annealing at 750°C for 2 h is shown in Ref. 20. These Pt electrodes turned out to be almost entirely blocking for oxygen exchange (see Results section) and thus allowed to gain information on both ionic and electronic charge carriers.

Sample preparation for Hebb-Wagner type polarization.—After sputtering a 400 nm Pt thin film on one side of the LSGM single crystal, as described above, a $\text{La}_{0.6}\text{Sr}_{0.4}\text{CoO}_{3-\delta}$ (LSC) layer was deposited on the back side of the sample by pulsed laser deposition (PLD). The LSC target preparation for PLD is described elsewhere.²¹ For the pulsed laser deposition, the substrate was heated to ~600°C in $4 \cdot 10^{-2}$ mbar

*Electrochemical Society Member.

^zE-mail: ghislain.rupp@tuwien.ac.at

pO_2 and the substrate to target distance was set to 6 cm. Ablation of the target material was carried out by a KrF ($\lambda = 248$ nm) excimer laser (Lambda COMPexPro 201F, Coherent, Germany) operated at a pulse repetition rate of 5 Hz, a pulse duration of 50 ns and a laser fluence of approximately $1.5 \text{ J} \cdot \text{cm}^{-2}$ at the target. By applying 1,025 laser pulses to the LSC target a thin film of approx. 50 nm thickness was grown on the substrate. After deposition, the sample was cooled in the same atmosphere at a cooling rate of $12^\circ\text{C} \cdot \text{min}^{-1}$.

Afterwards, a lift-off photolithographic process step was used to fabricate a current collector grid (35 μm mesh size, 15 μm stripe width) from a 5 nm Ti (ÖGUSSA, Austria) and 100 nm Pt thin film, sputtered on top of the LSC layer at room temperature in $7 \cdot 10^{-3}$ and $2 \cdot 10^{-2}$ mbar Ar atmosphere. The Ti between the LSC and Pt film acted as an adhesive layer. Finally, the side faces of the LSGM single crystals were grinded to remove any residual Pt or LSC. The LSC layer with current collectors acted as a reversible electrode with low oxygen exchange resistance.²¹

Structural characterization.—Diffraction patterns of the LSGM single crystal with and without LSC thin film as well as reciprocal space maps were obtained using a diffractometer (D8-Discover, Bruker AXS, Germany) in parallel beam geometry equipped with a general area detector diffraction system (GADDS). One LSGM single crystal was powderized in a tungsten carbide mortar and analyzed in Bragg Brentano geometry by a powder diffractometer (X'Pert Powder, PANalytical, Netherlands).

Sample setup and electrochemical measurements.—All annealing and impedance experiments were performed in a cleaned quartz tube which was evacuated and refilled several times with a 79% N_2 (ALPHAGAZ 1 >99.999 mol% nitrogen, Air Liquide, Austria)/21% O_2 (ALPHAGAZ 1 >99.998 mol% oxygen, Air Liquide) mixture before the sample was uniformly heated in a tube furnace. Samples were sandwiched between two platinum foils for the impedance and DC polarization experiments. Temperature series from $180^\circ\text{C} \rightarrow 800^\circ\text{C} \rightarrow 180^\circ\text{C} \rightarrow 800^\circ\text{C}$ with 50°C step size were used in the AC experiment. When the temperature or atmosphere was changed the sample was given at least 1/2 h to equilibrate before any measurements were started. Absence of any significant time dependence suggest equilibration with the gas atmosphere in all measurements. Oxygen partial pressure variations were performed from $550\text{--}800^\circ\text{C}$ and were archived by different high purity N_2/O_2 or $N_2/0.99\%O_2$ (pre-mixture of $0.99 \pm 0.02\%O_2$ in N_2 , Air Liquide) mixtures using mass flow controllers. The pO_2 was measured by a lambda probe (Micropoas, Setnag, France) placed in the vicinity of the specimen.

Impedance measurements were performed using an impedance analyzer (Alpha A High Performance Frequency Analyzer with a POT/GAL 30 V 2 A Test Interface, Novocontrol, Germany) in the frequency range from 10^6 Hz to a minimum of $5 \cdot 10^{-3}$ Hz with a resolution of five points per decade and an alternating voltage of 10 mV

(rms) applied between the two electrodes. The impedance spectra were quantitatively evaluated by a complex nonlinear least square fit program (Z-View2, Scribner, USA). The equivalent circuits used to fit the experimental data are shown in the respective sections. The serial 2-point Pt wire resistance was separately measured and taken into account in the equivalent circuit fits (not explicitly shown). It was determined by a temperature cycle without any sample, i.e. with the two Pt foils being in contact. The same measurement setup, including the potentiostat as DC voltage source, was also used in the Hebb-Wagner type polarization experiments.

Results

Structural characterization.—LSGM single crystals were examined in Bragg-Brentano Θ – 2Θ geometry using parallel-beam optics without and with additional 50 nm LSC thin film layer on top (sample for Hebb-Wagner polarization experiment). The diffraction patterns over the measured 2Θ range are shown in Fig. 1a. Furthermore, a diffraction pattern of a powderized LSGM single crystal (black) measured with focusing optics is shown in the figure. All peaks were indexed with respect to the pseudo-cubic structure of both materials and no sign of impurities was found. However, LSGM shows an orthogonally and LSC a rhombohedral distortion at room temperature. The orthorhombic structure of LSGM is clearly observed in the powder diffraction pattern by a peak at $38.2^\circ 2\Theta$ and splitting of other indexed peaks. The refined values of the calculated unit cell are $a = 7.782 \text{ \AA}$, $b = 5.493 \text{ \AA}$, $c = 5.533 \text{ \AA}$ and close to the values reported in Ref. 12 measured on $La_{0.95}Sr_{0.05}Ga_{0.9}Mg_{0.1}O_{3-\delta}$.

The LSC thin film deposited on the LSGM single crystal showed only [001] peaks in the measured 2Θ range and the epitaxial growth was further analyzed by a reciprocal space map, see Fig. 1b. The reciprocal space map shows a high intensity spot representing the $[-103]$ lattice plane of LSGM and two horizontally shifted satellite spots indicating different domains in the single crystal. This was also found in $La_{0.95}Sr_{0.05}Ga_{0.9}Mg_{0.1}O_{3-\delta}$ single crystals.^{7,22} The $[-103]$ lattice plane of LSC is observed directly above the high intensity LSGM spot. Thus, it can be concluded that the in-plane lattice components match well. A pseudo-cubic in-plane lattice parameter of $a_{pc, \parallel} = 3.87 \pm 0.01 \text{ \AA}$ for both materials and an out-of-plane lattice parameter of $a_{pc, \perp} = 3.90 \pm 0.01 \text{ \AA}$ and $a_{pc, \perp} = 3.80 \pm 0.01 \text{ \AA}$ results for LSGM and LSC, respectively. Hence, a tensile in-plane lattice strain of 1.1% can be determined based on the lattice mismatch between the strained LSC thin film and a relaxed LSC thin film ($a_{pc} = 3.838 \text{ \AA}$ ²¹) grown on YSZ. Although the strain induced in the electrode thin film is of minor importance in this work, deposition of perovskite-type materials on top of LSGM single crystals might be a very attractive strategy to investigate the influence of strain in thin film electrodes on the oxygen exchange and transport kinetics by means of electrical measurements (e.g. impedance spectroscopy).

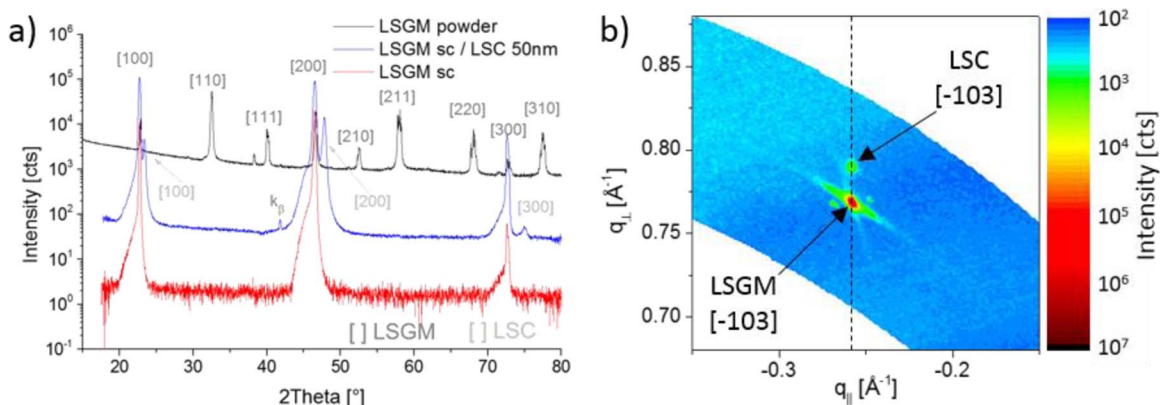


Figure 1. (a) XRD patterns of LSGM powder (black), an LSGM single crystal (blue) and an LSGM single crystal with an additional 50 nm thin LSC film on top (red). (b) XRD reciprocal space map showing the reflection of the $[-103]$ plane of both the LSGM substrate and 50 nm thin LSC film.

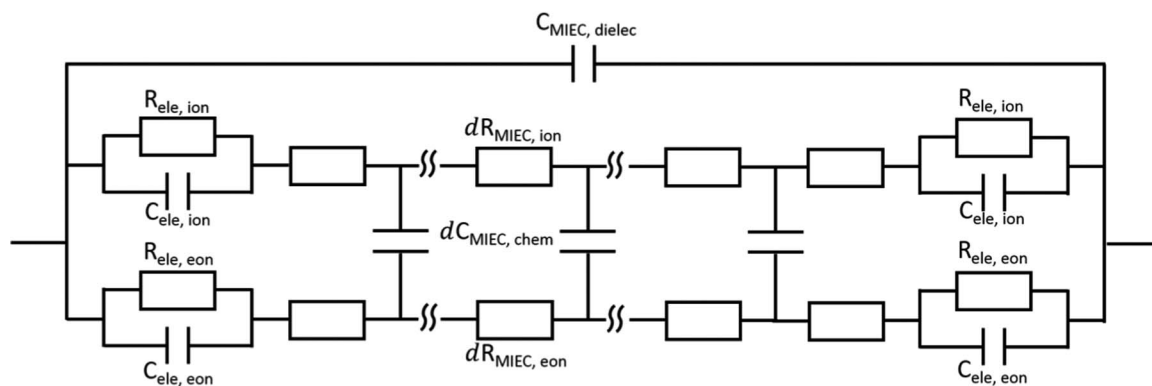


Figure 2. General equivalent circuit of a mixed ionic electronic conductor between two electrodes. In the data analysis software this circuit (except $C_{\text{MIEC, dielec}}$) is termed DX Type 19 - Jamnik-Maier-Lai-Lee.

Equivalent circuit model.—The general equivalent circuit model of a MIEC introduced by J. Jamnik and J. Maier,¹⁷ see Fig. 2, consist of an ionic and an electronic rail with a capacitive displacement rail in parallel to the entire circuit ($C_{\text{MIEC, dielec}}$ = geometrical capacitance of the MIEC). This circuit represents a homogenous MIEC under the assumption of local electroneutrality. The charge carrier flux in the bulk of the MIEC is determined by differential resistive elements along the ionic and electronic resistive rails, which are coupled by the chemical capacitance. The chemical capacitance describes the ability of a material to store chemical energy by undergoing stoichiometric changes. The ionic and electronic resistive rails are terminated on both sides by an RC-element to account for electrochemical reactions and charge transfer taking place at interfaces. Certainly, electrode reactions are very complex and may not necessarily be represented by this simplified terminal. However, all measurements could even be described by a capacitance $C_{\text{Pt, ion}}$ solely, i.e. consideration of a finite oxygen exchange resistance $R_{\text{ele, ion}}$ was not required. This already strongly suggests that the oxygen exchange reaction is essentially blocked at our Pt electrodes. Moreover, also the consistency of all interpretations

and quantities shown in the following (shape of the spectra, $p\text{O}_2$ dependence and activation energy of the derived electronic conductivity, shape of the current voltage curve) indicate that the assumption of virtually ion blocking electrodes is justified. Since, Pt electrodes were deposited on both sides of the LSGM single crystal, a symmetrical electrochemical cell was obtained and for the AC experiments only one half of the equivalent circuit from Fig. 2 is shown to highlight the relevant fit elements. Subscripts ele and MIEC are then specified by the given materials Pt and LSGM.

AC impedance measurements.—*Temperature dependence of the spectra shape.*—The temperature dependency of the impedance response was measured between 180°C and 800°C in synthetic air (mixture of 21% O_2 in N_2). Representative Nyquist plots starting from high temperatures and going to low temperatures in steps of $\sim 50^\circ\text{C}$ are shown in Figs. 3 and 4. The experimental data were fitted to the equivalent circuits shown below each plot. Fit elements and current paths of the entire circuit that were excluded in the particular temperature regime are indicated by dashed lines. An excellent

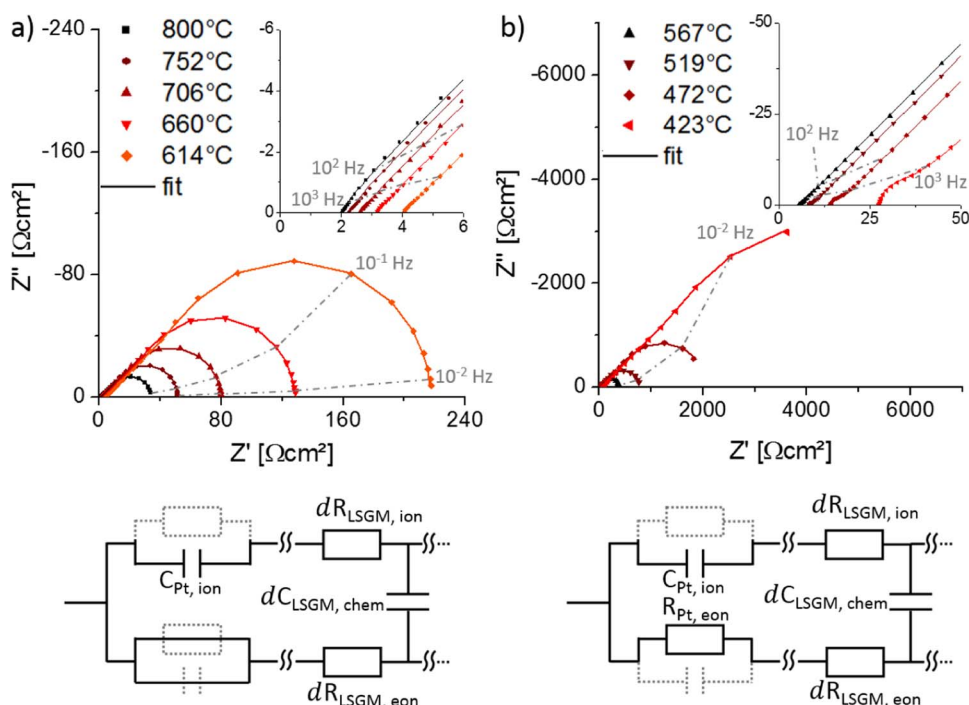


Figure 3. Nyquist plots of a Pt|LSGM|Pt sample measured at (a) 800–614°C and (b) 567–423°C in synthetic air. The respective equivalent circuits used to fit the experimental data are shown below the Nyquist plots. Grey dotted current paths and/or elements were omitted for the fit.

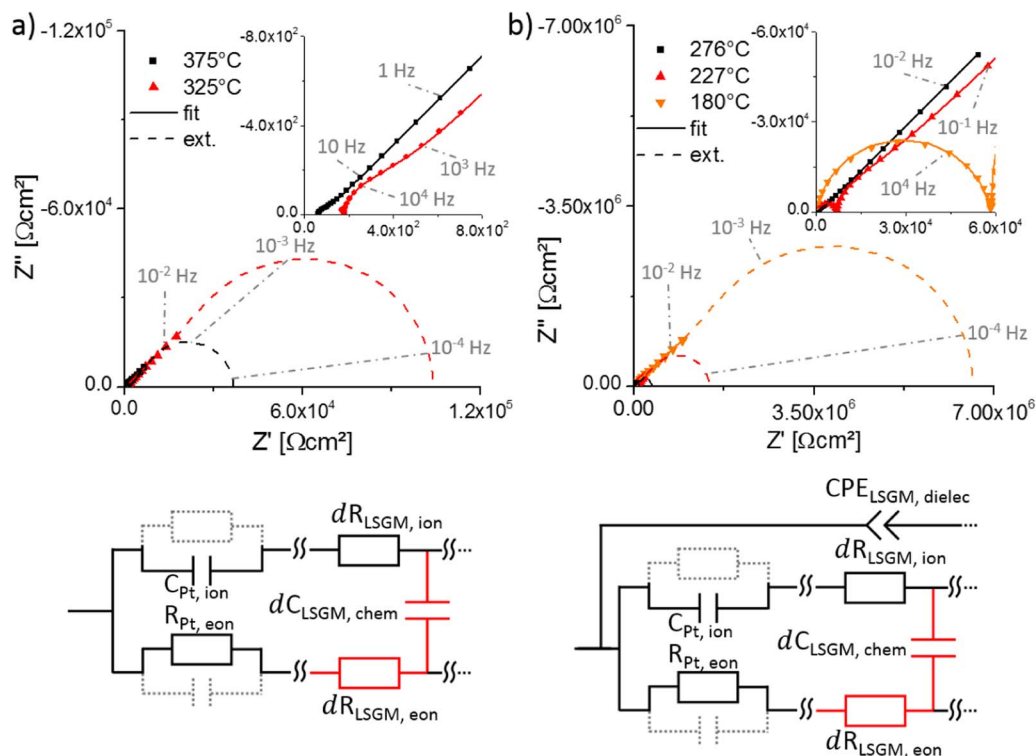


Figure 4. Nyquist plots of a Pt|LSGM|Pt sample measured at (a) 375–325°C and (b) 276–180°C in synthetic air. The respective equivalent circuits used to fit the experimental data are shown below the Nyquist plots. Grey dotted current paths and elements were omitted for the fit. Red highlighted equivalent circuit elements indicate that these quantities could only be determined with limited accuracy.

agreement between the presented equivalent circuit fitting model (solid line) and measured data (points) is found over the whole temperature range.

At high temperatures (800°C–614°C) the impedance spectra are characterized by a high frequency intercept and a semi-tear drop shaped feature, a Warburg-type impedance. After subtracting the serial wire resistance, the high frequency intercept (R_{hf}) corresponds to the total conductivity of the LSGM bulk, i.e. the electronic conductivity in parallel to the ionic conductivity, since the low impedance of the electrode capacitance ($C_{Pt,ion}$) allows ion movement at these frequencies. At lower frequencies, ion motion in LSGM becomes more and more hindered since the Pt electrodes essentially block the oxygen exchange and thus the ions. Consequently, a Warburg-type impedance is obtained. This can be reflected in the equivalent circuit, by an infinitely large $R_{Pt,ion}$. It is shown in Ref. 17,18 that in such a case with $C_{ele,ion} \ll C_{MIEC,chem}$ the impedance of the entire circuit (except $C_{MIEC,dielec}$) is given by

$$Z = R_{hf} + R_W \frac{\tanh((i\omega T)^p)}{(i\omega T)^p} \quad [1]$$

The second term corresponds to the analytical expression of a finite Warburg impedance with resistance R_W and fit parameters T and p . An ideal Warburg element is obtained for $p = 0.5$, which then also allows to directly relate the fit parameter T with the sample thickness L to the one-dimensional chemical diffusion coefficient D_{chem}

$$T = \left(\frac{L}{2}\right)^2 = \frac{C_{MIEC,chem} (R_{MIEC,eon} + R_{MIEC,ion})}{4} \quad [2]$$

Chemical diffusion coefficients at different temperatures and oxygen partial pressures are calculated by this relationship at the end of this section. Indeed, the serial connection of a finite Warburg element and a resistor also fits our data, instead of the generalized impedance circuit used in the entire study (here without $R_{Pt,ion}$, $C_{Pt,eon}$ and $R_{Pt,eon}$).

In the temperature regime 567°C–423°C a new semicircular shaped feature (10³–10⁵ Hz) arises between the high frequency intercept and

the Warburg-type impedance, see inset Fig. 3b. The impedance of this semicircle increases continuously with decreasing temperature. This feature cannot be explained by the equivalent circuit elements of the MIEC bulk. Thus, it has to be associated with a change of the terminals, i.e. the electrode impedance. Analysis of the impedance spectra by the entire equivalent circuit model of Fig. 2 revealed that only an additional electrode resistance in the electronic rail can describe the observed phenomena (cf. Fig. 3b bottom). This resistance may either refer to the LSGM||Pt or to the Pt||Pt-contact sheet interface. One reasonable explanation would be the formation of PtO_x at the Pt||LSGM interface; PtO_x was reported to decompose at higher temperatures.^{23,24} In any case, the equivalent circuit fits the measured data very well over the entire frequency regime and allows to extract also $R_{Pt,eon}$.

Below 400°C, Fig. 4, the semi-tear drop shaped low-frequency feature could no longer be fully resolved within a reasonable time (>1/2 hour for a single impedance spectra). Therefore only the first part, the Warburg-type diffusion slope, could be used to fit the experimental data and the quantities $R_{LSGM,eon}$ and $C_{LSGM,eon}$ were determined with less accuracy (highlighted in red in the equivalent circuit). The relative fitting error of these two parameters strongly increased from ~4% at 375°C to ~120% at 180°C. The latter error is still surprisingly “low” since at 180°C only about 1/7th of the real part of the Warburg-type element is measured. Extrapolations of the fitted impedance according to the equivalent circuit models (dashed lines) are shown in Fig. 4. At low temperatures (<276°C) the high frequency intercept changes into a high frequency semicircle, see inset. Its peak frequency $\omega = (RC)^{-1}$ is determined by the parallel elements $R_{LSGM,eon} || R_{LSGM,ion} || C_{LSGM,dielec} \approx R_{LSGM,ion} || C_{LSGM,dielec}$ and shifts into the measured frequency range because of the strong temperature dependence of $R_{LSGM,ion}$. A constant phase element instead of the capacitance $C_{LSGM,dielec}$ is used to fit the data properly. Its impedance is given by

$$Z_{CPE} = \frac{1}{T(i\omega)^p} \quad [3]$$

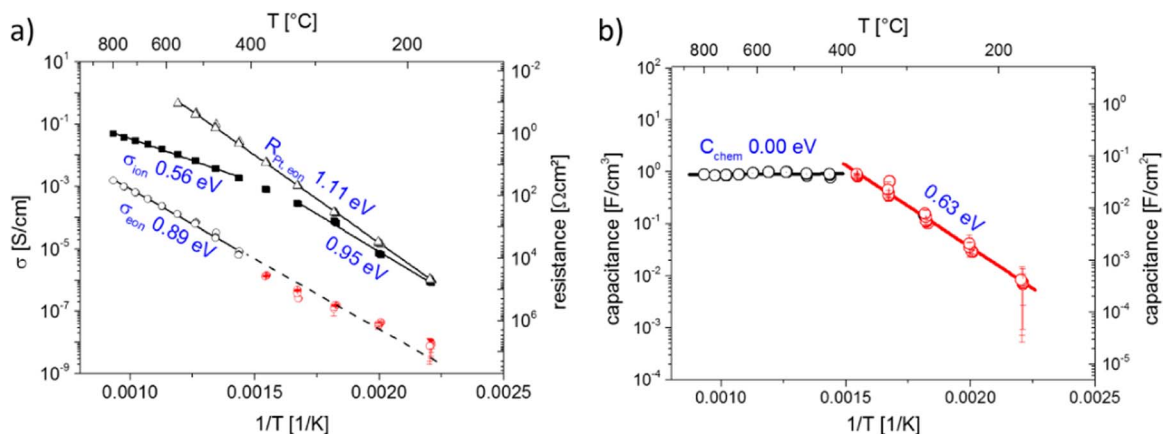


Figure 5. Arrhenius plots of the (a) resistive and (b) capacitive quantities of a Pt|LSGM|Pt sample measured in synthetic air. Red data points highlight measurements of limited accuracy (cf. Fig. 4 and error bars). Activation energies determined from the give data are also shown.

with the fitting parameters T and p . The capacitance was calculated by the relationship²⁵

$$C = (R^{1-p} \cdot T)^{1/p}. \quad [4]$$

For all measurements p -values of ~ 0.88 were obtained for the $CPE_{LSGM,dielec}$ element.

In this manner, all spectra could be quantified by one and the same generalized equivalent circuit model and four important materials parameters could be obtained: ionic conductivity (σ_{ion}), electronic conductivity (σ_{eon}), chemical capacitance (C_{chem}) and electronic interfacial resistance ($R_{Pt,eon}$). The other fit parameters ($C_{LSGM,dielec}$, $C_{Pt,ion}$) were also determined but are not discussed in detail.

Temperature dependence of the materials parameters.—Arrhenius plots of the resistances and the LSGM chemical capacitance extracted from three temperature series ($180^\circ\text{C} \rightarrow 800^\circ\text{C} \rightarrow 180^\circ\text{C} \rightarrow 800^\circ\text{C}$) are shown in Fig. 5 together with their activation energies. Values of all three series are in excellent agreement. Also two spectra measured for each temperature in each series with 30 minutes time difference did not show any time dependencies or hysteresis effects. Hence, we suppose that all values in Fig. 5 are equilibrated values. The ionic conductivity σ_{ion} of LSGM does not exhibit a simple linear Arrhenius-type behavior. A remarkable curvature is found with lower activation energies (0.56 eV) at higher temperatures. A changing activation energy was already observed for polycrystalline LSGM pellets of the same and other compositions as well as for other highly doped ionic conductors such as YSZ and GDC. It is generally explained by defect-dopant interactions such as trapping of isolated oxygen vacancies or formation of ordered-vacancy clusters at low temperatures. K. Huang et al.²⁶ experimentally found a strong correlation between the low temperature activation energy and the Mg concentration in $La_{1-x}Sr_xGa_{1-y}Mg_yO_{3-\delta}$ (and only minor influence of the Sr concentration). This is consistent with theoretical calculations of M. S. Islam²⁷ who determined a high binding energy for the $Mg_{Ga}^I - V_O^\bullet$ cluster compared to $Sr_{La}^I - V_O^\bullet$.

For the electronic conductivity an activation energy of 0.89 eV was determined between $423\text{--}800^\circ\text{C}$. The electronic conductivities determined for lower temperatures ($<400^\circ\text{C}$) are less accurate (see above) and analyzing only those values suggest a lower activation energy. However, extrapolating the accurate temperature values to low temperatures showed very reasonable agreement with measured data. Hence we suppose that the entire temperature range shows the same activation energy ca. 0.9 eV. The electronic transference number t_{eon} ($= \sigma_{eon}/(\sigma_{eon} + \sigma_{ion})$) has a minimum (0.001) at 320°C and increases at higher temperatures to 0.03 at 800°C in synthetic air. $R_{Pt,eon}$, finally, shows an ideal linear Arrhenius-type behavior with an activation energy of 1.11 eV.

The temperature dependency of the chemical capacitance exhibits two well separated regimes. At low temperatures (below 400°C) it

increases with an activation energy of 0.63 eV. Above this temperature it is essentially constant. The chemical capacitance of LSGM given is given by²⁸

$$C_{chem} = 4e^2V \left(\frac{\partial \mu_O}{\partial c_O} \right)^{-1} = 4e^2V \left(\frac{\partial}{\partial c_O} (-\mu_V + 2z_{eon}\mu_{eon}) \right)^{-1} \quad [5]$$

with e being the elementary charge, V the sample volume, c_O the oxygen concentration and the chemical potentials μ_O , μ_V , μ_{eon} of oxygen, vacancies and main electronic charge carriers (with charge number z_{eon}), respectively. Usually, the chemical capacitance is dominated by the minority charge carrier. Since for LSGM, $R_{ion} < R_{eon}$ and the ionic mobility is generally much lower than the electronic mobility, it can be concluded that the electronic charge carriers (here holes) are the minority species. In the dilute limit ($C_{chem} = 4e^2Vc_h/kT$) with hole concentration c_h results from Eq. 5. Accordingly, C_{chem} and σ_{eon} should exhibit similar temperature dependences, with the conductivity additionally including a temperature dependence of the mobility. However, while for the electronic conductivity high and low temperature activation energy are in reasonable agreement, C_{chem} exhibits a drastic change around 400°C . Agreement of high and low temperature values of σ_{eon} excludes an artifact of an inaccurate fit that causes the surprising C_{chem} - T behavior. We therefore propose that additional defect chemical effects come into play. A substantial number of trapped holes might be present, which increases C_{chem} but does not contribute to σ_{eon} . But also by including traps into the analysis of Eq. 5 we were not able to explain the activation energy change of C_{chem} and thus further unknown factors, including redox active impurities, seem to affect the chemical capacitance. Accordingly, we could not determine absolute hole concentrations from C_{chem} . The quantities $C_{Pt,ion}$ ($6.02 \pm 0.32 \cdot 10^{-5} \text{F/cm}^2$) and $C_{LSGM,dielec}$ ($1.13 \pm 0.01 \cdot 10^{-10} \text{F/cm}^2$) are not plotted but remained constant over the measurable temperature regime.

Oxygen partial pressure dependence.—The oxygen partial pressure (p_{O_2}) was varied between 0.21 and 1013 mbar and impedance spectra were measured at different temperatures (550°C – 800°C). Representative Nyquist plots at 700°C are shown in Fig. 6. A clear dependence of the spectra on p_{O_2} without any time drift is found and indicates equilibration of LSGM to each novel p_{O_2} prior to the impedance measurement. The experimental data were fitted to the equivalent circuit in Fig. 3a. $R_{Pt,eon}$ was not required for these measurements and an excellent agreement between data and fit is found for all oxygen partial pressures. In accordance with the interpretation given above the sum of the high frequency intercept and the Warburg resistance corresponds to the electronic transport resistance of LSGM. The total conductivity of LSGM is represented by the high frequency intercept and dominated by the ionic transport. The high frequency intercept

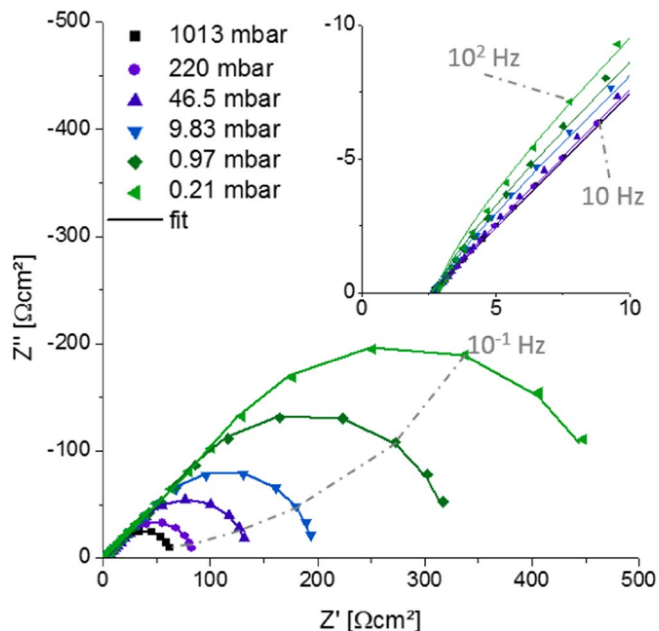
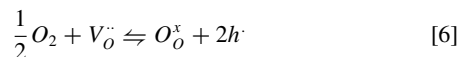


Figure 6. Nyquist plots of a Pt|LSGM|Pt sample measured at 700°C and different oxygen partial pressures. Experimental data were fitted to the equivalent circuit shown in Fig. 3a.

($\sim 2.7 \Omega\text{cm}^2$ for all $p\text{O}_2$) and thus σ_{ion} is essentially $p\text{O}_2$ independent. On the other hand, the size of the Warburg-type impedance increases significantly with decreasing $p\text{O}_2$. Accordingly, the electronic conductivity of LSGM shows a significant dependence on the oxygen partial pressure. This is quantitatively shown in Fig. 7a.

The slopes found for the electronic conductivity in such $\log \sigma$ – $\log p\text{O}_2$ diagrams are very close to 0.25 for all temperatures. Hence, the LSGM single crystals follow almost ideally the defect chemical model given by the following defect equilibrium:



$$[h^{\cdot}] = p\text{O}_2^{1/4} \cdot \sqrt{\frac{K_\text{o} \cdot [\text{V}_\text{O}^{\cdot\cdot}]}{[\text{O}_\text{O}^x]}} \quad [7]$$

The oxygen vacancy concentration $[\text{V}_\text{O}^{\cdot\cdot}]$ is essentially fixed by the dopant concentration in accordance with the $p\text{O}_2$ independent ionic conductivity and a slope of 0.25 should thus result. As a consequence,

the ionic transference number $t_{\text{ion}} (= \sigma_{\text{ion}} / (\sigma_{\text{eon}} + \sigma_{\text{ion}}))$ increases for lower oxygen partial pressures and for lower temperatures. Electronic conductivities are often determined by the Hebb-Wagner method (see Hebb-Wagner type polarization section) and this also reveals information on the $p\text{O}_2$ dependence of σ_{eon} (or, more precisely, its dependence on the oxygen chemical potential). The beauty of the impedance approach used here, however, is the fact that very accurate absolute conductivity values can be determined for each $p\text{O}_2$. This allows very precise analysis of slopes in $\log \sigma$ – $\log p\text{O}_2$ plots. In Hebb-Wagner measurements absolute electronic conductivities are generally obtained from a fit of an idealized model to a complete I - V curve (see below) and small deviations from ideality are easily missed. Alternatively, absolute values can be obtained from slopes of I - V curves, which is usually again a less accurate approach.

Fig. 7b displays the C_{chem} dependency on the oxygen partial pressure in a linear plot. A very clear general trend is not found. However, it can be excluded that only free electron holes determine the chemical capacitance, since the slope of C_{chem} does not match the slope of σ_{eon} . This again supports the assumption of a complex interplay of defect chemical effects in C_{chem} already discussed above. The oxygen chemical diffusion coefficient of LSGM D_{chem} was determined according to Equation 2, see Fig. 8. This reveals a $p\text{O}_2$ dependence and in particular a surprising temperature dependence. But a simple interpretation of the latter, especially of its temperature independent part, is not possible due to the complex nature of C_{chem} . Still D_{chem} values are in accordance with our assumption of equilibrated LSGM samples at all temperatures.

Comparison with literature data on partial conductivities of polycrystalline LSGM.—The ionic conductivity of polycrystalline LSGM samples with various compositions was investigated between 150–400°C by several authors using AC impedance measurements.^{1,9,29,30} Typically, two semicircles representing the grain and grain boundary resistance of the electrolyte material are observed in the Nyquist plot and the conductivity can thus be separately determined for both. At higher temperatures, peak frequencies of the two arcs are increased and exceed the measurement limit of most impedance analyzers (> 10 MHz), which then only allows determining the total ionic conductivity. However, the absolute values obtained for the ionic conductivity of our LSGM single crystal are in excellent agreement with measurements of the total conductivity on polycrystalline pellets of the same composition at temperatures of 595–800°C.²⁶ Our results therefore confirm that the ionic conductivity measured in Ref. 26 indeed represents the bulk conductivity and that the grain to grain boundary conductivity ratio of those samples has to be much smaller than the thickness ratio of grain to grain boundary.³¹

In Oxygen partial pressure dependence section it was shown that in the given oxygen partial pressure regime holes are responsible for the electronic conductivity. Our activation energy (0.89 eV)

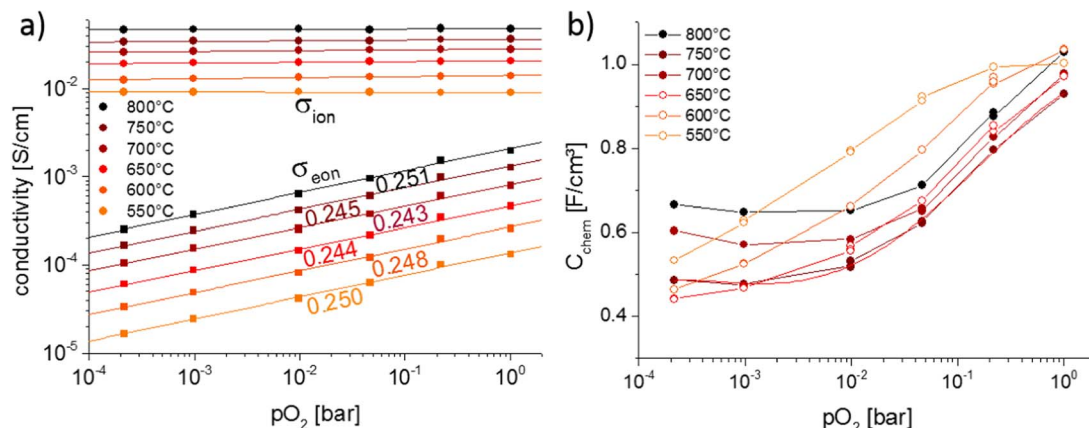


Figure 7. Oxygen partial pressure dependence of the (a) conductivities and (b) the chemical capacitance of a Pt|LSGM|Pt sample between 550–800°C. Power laws according to $\sigma_{\text{eon}} \sim (p\text{O}_2)^m$ are indicated in (a) together with their linear fit (solid lines). The solid lines in (b) only represent a guide to the eye.

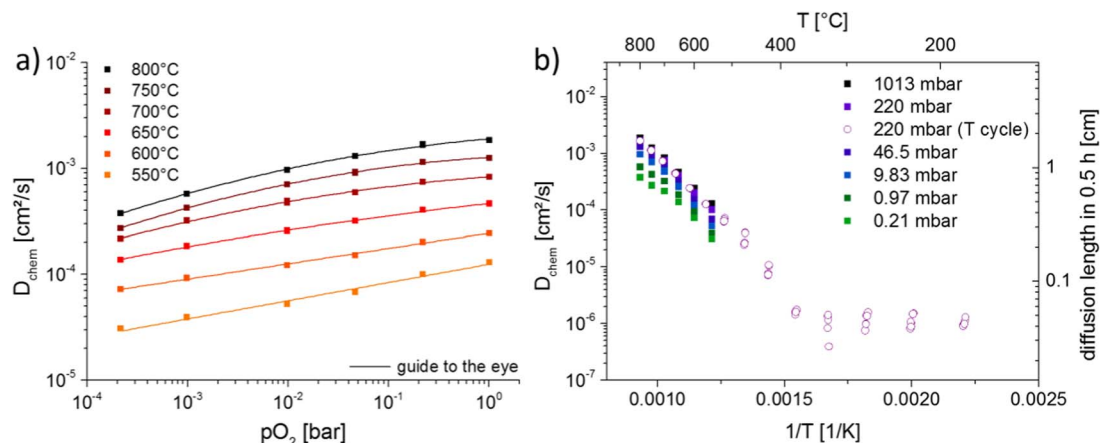


Figure 8. (a) Oxygen partial pressure and (b) temperature dependence of the oxygen chemical diffusion coefficient of a LSGM single crystal. Diffusing lengths calculated from $(D_{\text{chem}} \cdot t)^{1/2}$, $t = 0.5$ h, are also indicated.

can thus be compared to the values reported for measurements of the p-type conductivity in $\text{La}_{0.9}\text{Sr}_{0.1}\text{GaO}_{3-\delta}$ ³² (0.86 eV) and $\text{La}_{0.9}\text{Sr}_{0.1}\text{Ga}_{0.8}\text{Mg}_{0.2}\text{O}_{3-\delta}$ ⁵ (1.12 eV) performed by ion-blocking DC techniques (cf. Hebb-Wagner type polarization section). Activation energies are similar, despite some differences in the exact LSGM composition. However, the electronic conductivity measured in our study (e.g. $1.5 \cdot 10^{-3}$ S/cm at 800°C in syn. air) is a pure bulk property, while from measurements in literature, performed on polycrystals, only effective electronic conductivities are available. This makes a quantitative comparison difficult. Interestingly, literature data on the p-type conductivity show very pronounced differences ($3.6 \cdot 10^{-4}$ S/cm for $\text{La}_{0.9}\text{Sr}_{0.1}\text{Ga}_{0.8}\text{Mg}_{0.2}\text{O}_{3-\delta}$, $5 \cdot 10^{-4}$ S/cm for $\text{La}_{0.9}\text{Sr}_{0.1}\text{GaO}_{3-\delta}$ ³² and $3.6 \cdot 10^{-3}$ S/cm for $\text{LaGa}_{0.85}\text{Mg}_{0.15}\text{O}_{3-\delta}$ ³³ at 800°C in air and $3.1 \cdot 10^{-6}$ S/cm for $\text{La}_{0.95}\text{Sr}_{0.05}\text{GaO}_{3-\delta}$ ³⁴ at 767°C in 1.013 bar O_2). This is not expected from a simple defect chemical model despite some differences in the Sr and Mg doping concentrations: In all compositions (including ours) effective acceptor doping and thus also oxygen vacancy concentrations differs at most by a factor of six and according to Equation 7 the hole conductivities should thus differ by at most $\sqrt{6} = 2.45$. Reported differences are much larger and also do not show a systematic trend with doping concentration. This suggests that effective electronic conductivities of polycrystals being much lower than those of our single crystals are at least partly affected by grain boundary effects. Presumably grain boundaries are more blocking for electrons than for ions and can substantially lower the effective electronic conductivity.

Hebb-Wagner type polarization.—For reasons of comparison the p-type and n-type conductivities were also determined in a Hebb-Wagner type polarization experiment. This method is more frequently used than the AC approach shown above and also all literature data of σ_{eon} in LSGM available so far were obtained in that manner. For these measurements the electrode arrangement has to be changed. A 50 nm thin LSC film was deposited on one side of the LSGM single crystal and a Pt mesh (35 μm mesh size) was sputtered on top of the film to avoid in-plane sheet resistances in the LSC film. LSC is expected to act as an almost reversible electrode for oxygen exchange.²¹ A 400 nm thin Pt electrode (as used in AC experiments) on the other side of the specimen served as ion blocking electrode. The experiment was performed at 600°C and 0.21 bar pO_2 . A bias voltage between -0.1 and 1.7 V (100 mV step size) was applied to the reversible LSC electrode relative to the blocking electrode. The current-voltage characteristics of the cell is shown in Fig. 9a (currents measured 10 minutes after each voltage change).

Small negative voltages lead to a strong current increase. For positive voltages the current increase becomes rather small except for

$U > 1.5$ V. The relation between current and voltage in ion-blocking polarization experiment was first described by Hebb and Wagner in Refs. 35,36 Supposing exact validity of Eq. 7 and band-band equilibrium $[e^{\cdot}] \cdot [h^{\cdot}] = K_e$ as well as $[e^{\cdot}] \cdot [h^{\cdot}] \ll [V_{\text{O}^{\cdot-}}]$ for all chemical potentials, it is given by

$$I = \frac{RT}{F} \cdot \frac{A}{L} \left(\sigma_p \left[1 - e^{-\frac{UF}{RT}} \right] + \sigma_n \left[e^{\frac{UF}{RT}} - 1 \right] \right) \quad [8]$$

with R being the universal gas constant, T the temperature, F the Faraday constant, A and L the sample area and thickness, respectively. The hole conductivity σ_p and the electron conductivity σ_n at the reference partial pressure (0.21 bar pO_2 , in this case) can be determined by fitting the measured data to Equation 8. However, for very different σ_p and σ_n Eq. 8 should lead to an almost constant current in a large voltage range. This is in contrast to our data with a continuous slight increase between 0.3 and 1.3 V. Supposedly, an ionic leakage current is the reason for this non-ideality, since the side faces of the LSGM single crystal were not sealed and therefore allowed oxygen exchange. Similar non-idealities can also be found in literature.^{5,32,34,37}

To take account of this leakage current an additional linear term with slope α is introduced into Eq. 8 leading to

$$I = \frac{RT}{F} \cdot \frac{A}{L} \left(\sigma_p \left[1 - e^{-\frac{UF}{RT}} \right] + \sigma_n \left[e^{\frac{UF}{RT}} - 1 \right] \right) + \alpha U \quad [9]$$

and the fit to the measured data set is shown in Fig. 9a. The additional ohmic resistance α^{-1} determined from the fit is $2.7 \pm 0.1 \cdot 10^4 \Omega$. The excellent fit suggests indeed an ohmic resistor determining this leakage current despite supposed serial oxygen incorporation at Pt. However, from the agreement between AC results and defect chemical models (AC impedance measurements section) we conclude that AC experiments, although using the same ion blocking Pt electrodes, are virtually unaffected by such leakage currents. This is most probably due to the much stronger polarization in DC (up to 1.7 V) compared to the AC (0.01 V) experiments. A high voltage leads to a high μ_{O} step between gas phase and LSGM close to the Pt electrode and also to a higher electron concentration in LSGM close to the Pt electrode. Hence, there is a much larger driving force for oxygen incorporation in the DC experiments and an increased concentration of the electronic defects which may ease the oxygen incorporation. The voltage-induced high electron concentration in the electrolyte may even lead to an extension of the oxygen incorporation area from the triple phase boundary of Pt electrodes along parts of the free electrolyte surface; this was reported for YSZ electrolytes under strong cathodic bias in Ref. 38.

A p-type conductivity of $2.2 \pm 0.1 \cdot 10^{-4}$ S \cdot cm⁻¹ at 0.21 bar pO_2 is determined and this is in very good agreement with the total electronic conductivity (σ_{eon}) measured during pO_2 variation

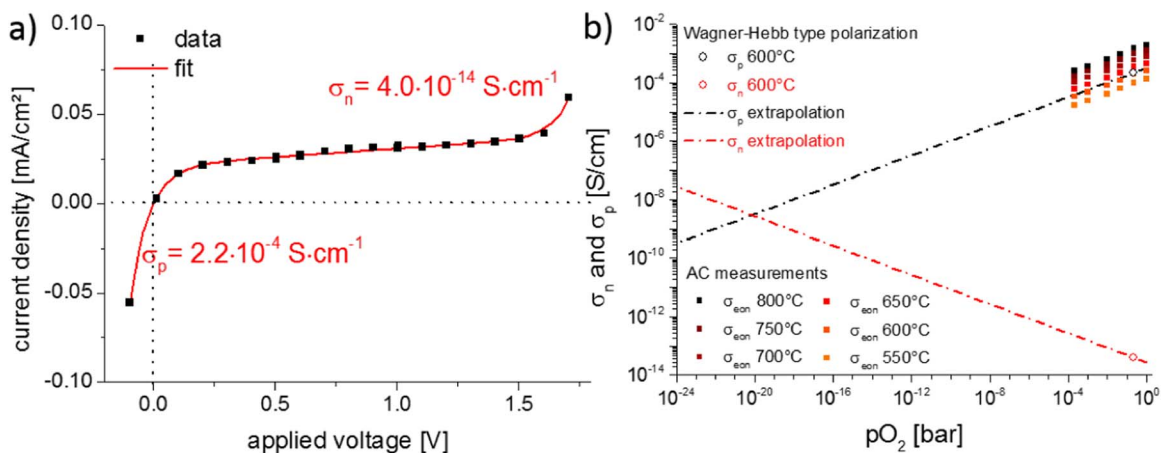


Figure 9. (a) Current–voltage characteristic of a Pt|LSGM|LSC sample at 600°C. The oxygen partial pressure at the reversible electrode (LSC) was set to 0.21 bar pO₂. The p- and n-type conductivities for zero voltage, determined by fitting the experimental data to Eq. 9, are highlighted red. (b) Brouwer type diagram of the p-type and n-type conductivity, including extrapolated values, measured by Hebb-Wagner type polarization and the total electronic conductivity measured in the AC experiment.

($1.9 \pm 0.1 \cdot 10^{-4} \text{ S} \cdot \text{cm}^{-1}$) and temperature cycling ($2.0 \pm 0.1 \cdot 10^{-4} \text{ S} \cdot \text{cm}^{-1}$) by the impedance approach shown above. The n-type conductivity of $4.0 \pm 0.2 \cdot 10^{-14} \text{ S} \cdot \text{cm}^{-1}$ obtained in this experiment is not accessible in the AC experiment. It may best be compared to extrapolated values from Ref. 34, $3.1 \cdot 10^{-13} \text{ S} \cdot \text{cm}^{-1}$ at 600°C in 1.013 bar pO₂. There, the n-type conductivity was also measured by an ion-blocking polarization technique but between 967–767°C on polycrystalline La_{0.95}Sr_{0.05}GaO_{3-δ} samples. The results of the electronic conductivity of LSGM are again summarized in a kind of Brouwer diagram in Fig. 9b. It includes precisely measured σ_{eon} data from AC experiments, the two fit values of hole (σ_p) and electron (σ_n) conductivity at 600°C in syn. air and lines representing conductivities according to the Hebb-Wagner measurements for ideal slopes of 0.25. At 600°C the hole conductivity equals the electron conductivity at an oxygen partial pressure of approx. 10^{-20} bar pO₂ with $\sigma_n = \sigma_p \approx 3 \cdot 10^{-9} \text{ S} \cdot \text{cm}^{-1}$.

Conclusions

An AC impedance study on La_{0.95}Sr_{0.05}Ga_{0.95}Mg_{0.05}O_{3-δ} (LSGM) single crystals with ion blocking electrodes was carried out and the impedance spectra were quantitatively evaluated over the entire measured temperature and pO₂ range by the general equivalent circuit model for mixed conductors. The excellent agreement between fit and experimental data allowed determination of the ionic and electronic conductivity, the chemical capacitance and the oxygen chemical diffusion coefficient from a single impedance spectrum. Activation energies for the electronic (0.89 eV) and ionic transport (0.95 eV at low and 0.56 eV at high temperatures) were calculated. Partial pressure as well as temperature dependence of the chemical capacitance suggests existence of trapped electronic defects and further defect chemical complexities. The p-type conductivity on the other hand was almost exactly proportional to pO₂^{1/4} in the range of 10⁻⁴ to 1 bar oxygen partial pressure and thus shows impressive agreement with ideal dilute defect chemical models. Hebb-Wagner type DC polarization experiments yielded a p- and n-type conductivity of $2.2 \pm 0.1 \cdot 10^{-4} \text{ S} \cdot \text{cm}^{-1}$ and $4.0 \pm 0.2 \cdot 10^{-14} \text{ S} \cdot \text{cm}^{-1}$ respectively at 600°C and 0.21 bar pO₂. DC results are in excellent agreement with those determined by the AC experiments under the same conditions. This supports the supposed reliability of the AC method to precisely determine electronic conductivities.

Acknowledgment

The authors gratefully acknowledge funding by Austrian Science Fund (FWF) project P4509-N16 and W1243-N16.

References

1. K. Huang, R. S. Tichy, and J. B. Goodenough, *Journal of the American Ceramic Society*, **81**(10), 2576 (1998).
2. C. Zuo, S. Zha, M. Liu, M. Hatano, and M. Uchiyama, *Advanced Materials*, **18**(24), 3318 (2006).
3. B. C. H. Steele and A. Heinzel, *Nature*, **414**(6861), 345 (2001).
4. T. Ishihara, H. Matsuda, and Y. Takita, *Journal of the American Chemical Society*, **116**(9), 3801 (1994).
5. J.-H. Kim and H.-I. Yoo, *Solid State Ionics*, **140**(1), 105 (2001).
6. C. Oncel, B. Ozkaya, and M. A. Gulgun, *Journal of the European Ceramic Society*, **27**(2-3), 599 (2007).
7. M. Kurumada, E. Iguchi, and D. I. Savvitskii, *Journal of Applied Physics*, **100**(1), 014107 (2006).
8. L. Cong, T. He, Y. Ji, P. Guan, Y. Huang, and W. Su, *Journal of Alloys and Compounds*, **348**(1-2), 325 (2003).
9. B. Rambabu, S. Ghosh, W. Zhao, and H. Jena, *Journal of Power Sources*, **159**(1), 21 (2006).
10. Z.-C. Li, H. Zhang, B. Bergman, and X. Zou, *Journal of the European Ceramic Society*, **26**(12), 2357 (2006).
11. V. Thangadurai and W. Weppner, *Electrochimica Acta*, **50**(9), 1871 (2005).
12. L. Vasylychko, V. Vashook, D. Savvitskii, A. Senyshyn, R. Niewa, M. Knapp, H. Ullmann, M. Berkowski, A. Matkovskii, and U. Bismayer, *Journal of Solid State Chemistry*, **172**(2), 396 (2003).
13. T. Van Dijk and A. Burggraaf, *Physica status solidi (a)*, **63**(1), 229 (1981).
14. J. C. C. Abrantes, J. A. Labrincha, and J. R. Frade, *Journal of the European Ceramic Society*, **20**(10), 1603 (2000).
15. M. Gerstl, E. Navickas, G. Friedbacher, F. Kubel, M. Ahrens, and J. Fleig, *Solid State Ionics*, **185**(1), 32 (2011).
16. J. Fleig and J. Maier, *Physical Chemistry Chemical Physics*, **1**(14), 3315 (1999).
17. J. Jamnik and J. Maier, *Physical Chemistry Chemical Physics*, **3**(9), 1668 (2001).
18. W. Lai and S. M. Haile, *Journal of the American Ceramic Society*, **88**(11), 2979 (2005).
19. J.-S. Lee, J. Jamnik, and J. Maier, *Monatshefte für Chemie - Chemical Monthly*, **140**(9), 1113 (2009).
20. A. K. Opitz, A. Lutz, M. Kubicek, F. Kubel, H. Hutter, and J. Fleig, *Electrochimica Acta*, **56**(27), 9727 (2011).
21. G. M. Rupp, A. Schmid, A. Nening, and J. Fleig, *Journal of The Electrochemical Society*, **163**(6), F564 (2016).
22. D. I. Savvitskii, D. M. Trots, L. O. Vasylychko, N. Tamura, and M. Berkowski, *Journal of Applied Crystallography*, **36**(5), 1197 (2003).
23. V. Stancovski, S. Sridhar, and U. B. Pal, *Journal of Electroceramics*, **3**(3), 279 (1999).
24. R. J. Berry, *Surface Science*, **76**(2), 415 (1978).
25. J. Fleig, *Solid State Ionics*, **150**(1-2), 181 (2002).
26. K. Huang, R. S. Tichy, and J. B. Goodenough, *Journal of the American Ceramic Society*, **81**(10), 2565 (1998).
27. M. Saiful Islam, *Journal of Materials Chemistry*, **10**(4), 1027 (2000).
28. J. Jamnik and J. Maier, *Journal of The Electrochemical Society*, **146**(11), 4183 (1999).
29. D. Marrero-López, J. Ruiz-Morales, J. Peña-Martínez, M. Martín-Sedeño, and J. Ramos-Barrado, *Solid State Ionics*, **186**(1), 44 (2011).
30. C. Haavik, E. M. Ottesen, K. Nomura, J. A. Kilner, and T. Norby, *Solid State Ionics*, **174**(1-4), 233 (2004).

31. J. Maier, *Berichte der Bunsengesellschaft für physikalische Chemie*, **90**(1), 26 (1986).
32. R. T. Baker, B. Gharbage, and F. M. B. Marques, *Journal of The Electrochemical Society*, **144**(9), 3130 (1997).
33. V. Kharton, A. Yaremchenko, A. Viskup, G. Mather, E. Naumovich, and F. Marques, *Solid State Ionics*, **128**(1), 79 (2000).
34. P. S. Anderson, F. M. B. Marques, D. C. Sinclair, and A. R. West, *Solid State Ionics*, **118**(3–4), 229 (1999).
35. C. Wagner, *Zeitschrift für Elektrochemie, Berichte der Bunsengesellschaft für physikalische Chemie*, **60**(1), 4 (1956).
36. M. H. Hebb, *The Journal of Chemical Physics*, **20**(1), 185 (1952).
37. J. H. Jang and G. M. Choi, *Solid State Ionics*, **154–155**, 481 (2002).
38. M. Kubicek, G. Holzlechner, A. K. Opitz, S. Larisegger, H. Hutter, and J. Fleig, *Applied Surface Science*, **289**, 407 (2014).